Journal of Turbulence

ISSN: (Print) 1468-5248 (Online) Journal homepage: http://www.tandfonline.com/loi/tjot20

Numerical investigation of free-stream turbulence effects on the transition-in-wake state of flow past a circular cylinder

J. R. Aarnes, H. I. Andersson & N. E. L. Haugen

To cite this article: J. R. Aarnes, H. I. Andersson & N. E. L. Haugen (2018) Numerical investigation of free-stream turbulence effects on the transition-in-wake state of flow past a circular cylinder, Journal of Turbulence, 19:3, 252-273, DOI: 10.1080/14685248.2017.1418085

To link to this article: https://doi.org/10.1080/14685248.2017.1418085

JOURNAL OF TURBULENCE, 2018
VOL. 19, NO. 3, 252–273
https://doi.org/10.1080/14685248.2017.1418085

Taylor & Francis
Taylor & Francis Group

Numerical investigation of free-stream turbulence effects on the transition-in-wake state of flow past a circular cylinder

J. R. Aarnes [a], H. I. Andersson [a] and N. E. L. Haugen [a,b]

[a]Department of Energy and Process Engineering, Norwegian University of Science and Technology, Trondheim, Norway; [b]SINTEF Energy Research, Trondheim, Norway

ABSTRACT

We investigate how a turbulent free-stream (TFS) affects the transition-in-wake state of flow past a cylinder. Direct numerical simulations of a decaying TFS flow past a cylinder have been performed, where the intensity and integral scale of the TFS was varied. Distinct effects of the TFS are observed for Reynolds numbers in the lower ($\mathrm{Re} < 190$) and upper ($\mathrm{Re} \geq 250$) ranges of the transitional regime. For a flow with a laminar free-stream (LFS), the onset of the transition-in-wake is observed at critical Reynolds number 190, where the first three-dimensional effects develop in the wake (mode *A* instabilities). A TFS perturbs the flow, forcing the onset of the transition at a lower Reynolds number and inhibiting a sharply defined critical Reynolds number. Quasi-stable states, where the wake alternates between two- and three-dimensional vortex shedding, are observed for $\mathrm{Re} < 190$. These states are closely related to intermittent vortex dislocations in the wake. In the upper Re part of the transition-in-wake regime, mode *B* instabilities dominate the wake of the LFS flow. A TFS stimulates the existence of mode *A* instabilities, resulting in mixed *A*–*B* instabilities in the wake for $\mathrm{Re} \geq 250$. This effect correlates with the turbulence intensity.

ARTICLE HISTORY
Received 28 June 2017
Accepted 28 November 2017

KEYWORDS
Isotropic turbulence; chaos and fractals; direct numerical simulation

1. Introduction

The unsteady vortex shedding and the transition to turbulence in flows past a circular cylinder have been an actively studied field of fluid mechanics during the last century. The flow problem has a generic nature and direct relevance to engineering applications.

The flow past a circular cylinder is steady at sufficiently low Reynolds numbers. The Reynolds number of the flow is defined as $\mathrm{Re} = \bar{U}D/\nu$, where $\bar{U}$ is the mean velocity of the flow, D is the diameter of the cylinder and ν is the kinematic viscosity. At $\mathrm{Re} \simeq 47$ the flow becomes unsteady by a Hopf bifurcation (see, e.g. [1]), which can be observed as oscillations in the wake of the cylinder. As the Reynolds number is increased, the characteristic von Kármán vortex street develops. The flow pattern of alternating vortices being shed from the cylinder is purely two-dimensional. With a further increase in the Reynolds number, the first three-dimensional effects can be observed in the flow. At this point, the flow past the cylinder is in the transition-in-wake state, which spans the range of Reynolds numbers:

CONTACT J. R. Aarnes jorgen.r.aarnes@ntnu.no

$(180 - 200) < \mathrm{Re} < (350 - 400)$ [2,3]. Following the transition-in-wake state of the flow, increasing Re leads to further break-up of the flow through several transitional regimes, before it can be characterised as fully turbulent.

The focus of this study is on the transition-in-wake state of the flow, and the effects that a turbulent free-stream (TFS) may have on this particular transition. Although it was noted above that this transition starts at $180 < \mathrm{Re} < 200$, there is considerable variation in the reported critical point where this transition first occurs (see [3], and references therein). We will henceforth denote this point the critical Reynolds number, abbreviated as Re_c for flow with laminar free-stream (LFS) and $\mathrm{Re}_{c,\,\mathrm{TFS}}$ for the TFS case. This is a *secondary instability* of the flow (opposed to the *primary instability* at $\mathrm{Re} \simeq 47$ [4]), and other authors may use Re_2, $\mathrm{Re}_{\mathrm{tr}}$, etc. to denote the onset of this instability. We will not consider the primary instability any further and therefore find Re_c to be an appropriate notation for the Reynolds number at onset of the transition-in-wake state of the flow.

By Floquet stability analysis, Barkley and Henderson [4] could identify the onset of transition at $\mathrm{Re}_c = 189$ and Henderson and Barkley [5] further proved that the transition is subcritical, explaining the hysteresis effect observed experimentally [6]. For $\mathrm{Re} \gtrsim 189$, three-dimensional modes with spanwise length of approximately four cylinder diameters develop in the flow. These mode *A* instabilities [6,7] are the dominant flow features in the spanwise direction in the first part of the transition-in-wake regime, along with spot-like *vortex dislocations*. The vortex dislocations are large-scale intermittent structures that grow downstream of the cylinder. These dislocations were discovered experimentally by Williamson [8], and similar features have been reproduced in numerical simulations (see [9,10]). Zhang et al. [9] call these structures vortex adhesion, due to vortices evidently adhering to the cylinder over many shedding periods, and found them to be self-sustained in the range $160 < \mathrm{Re} < 230$. Henderson [10] points out that the spot-like dislocations must be generated by the mode *A* instability, and concludes that a nonlinear interaction between self-excited modes in the *A*-band is responsible for the appearance of large-scale structures in the wake. Here, the *A*-band refers to the different possible wavelengths of the mode *A* instability. The observed spanwise wavelength of the three-dimensional pattern developing in the wake corresponds to the most unstable wavelength of the *A*-band. The wavelength is $\lambda_A \approx 4D$ at Re_c, decreasing somewhat as Re is increased (details in [4], Figure 12). Through high accuracy numerical simulations, Posdziech and Grundmann [11] reproduced the transition-in-wake with excellent agreement with experimental results. By using a spanwise domain length equal to the most unstable mode *A* instability the authors claim to exclude vortex dislocations in the wake, and conclude therefore that the role of such dislocations are overrated in experimental studies of the transitional regime.

When the Reynolds number is further increased, a new mode of instabilities develops in the wake: mode *B* instabilities. These instabilities are streamwise structures with spanwise length of approximately one cylinder diameter, dominating the flow at $\mathrm{Re} \gtrsim 260$ (see [7] and references therein). At Reynolds numbers between 210 and 220 the mode *A* and mode *B* instabilities start to coexist in the wake. The transition from a flow dominated by one mode to dominance of the other is gradual, with energy in the flow shifting continuously from the larger to the smaller instabilities (see, e.g. [12]) over a range of Reynolds numbers. Note that unlike the transition where mode *A* instabilities first occur, the second transition in the transition-in-wake state of the flow is supercritical [12].

The onset of the three-dimensional transition-in-wake can be identified by a sharp drop in the Strouhal number as Re is increased. The Strouhal number is defined as $\mathrm{St} = fD/\bar{U}$, where f is the vortex shedding frequency. The drop in St is observed at the onset of the subcritical instability where the first mode *A* instabilities develop in the cylinder wake. As mode *B* instabilities start to develop alongside of the mode *A* instabilities, the shedding frequency is gradually increased towards that of the two-dimensional shedding state. As already mentioned, there is a considerable scatter in the reported critical Reynolds number where this St drop occurs. This is especially prominent in experimental results, which can be seen by comparing data from e.g. Gerrard [13], Williamson [6] and Norberg [14], where Re_c-values between 140 and 200 are reported. This point should be kept in mind when studies where the effect of free-stream turbulence upstream of the cylinder in the transitional regime are considered. The effect of TFS may have been overrated by some authors and underrated by others in previous studies, due to other disturbances (e.g. contamination from end conditions).

In studies performed in two different wind tunnels, Bloor [15] found a significant effect of TFS on the critical Reynolds number. The experiments were performed with low turbulence intensity, $T_i = u_{\mathrm{rms}}/\bar{U} = 0.03\%$ and 1% (where u_{rms} is the root-mean-square value of the three-dimensional velocity fluctuations). Instabilities developed in the wake for Re between 160 and 200, where the higher Re consistently corresponded to the experimental set-up with the lowest turbulence intensity. How large the contribution of, e.g. end conditions was on the onset of transition in these experiments is hard to say, but it cannot be ruled out as an influencing parameter in the experiments, since the different turbulence intensities correspond to different experimental rigs in this study. Hussain and Ramjee [16] studied the effect of TFS on the shedding frequency at Reynolds numbers in the range of the von Kármán vortex street. The experiments were performed for $60 < \mathrm{Re} \lesssim 160$ and T_i up to 8%. No effect of the TFS on the flow was found. This result has been used to argue that the transition-in-wake state of the flow is insensitive to TFS [17]. This is not a valid argument, since Hussain and Ramjee [16] only considered Re below the Re_c reported in the majority of studies on the subject. In a study by Norberg [18], flow past a cylinder for a large Re span was investigated, and the flow was deemed 'rather insensitive' to low intensity, free-stream turbulence ($T_i = 1.4\%$) for $50 < \mathrm{Re} < 10^3$. Norberg [18] did, however, find an increase in the relative bandwidth of Re spanning the transitional regime, thereby supporting the observations by Bloor [15].

Beyond the investigations mentioned here, there exist few studies on the effect of TFS on the transition-in-wake state of the flow past a circular cylinder. To the best of our knowledge, no such studies have been performed using direct numerical simulations (DNS) as the main research tool. An advantage of DNS is that the end conditions, turbulence intensity, etc. can be kept exactly the same in all the simulations. This makes it an ideal tool for further investigations of the effect of TFS on the transition-in-wake, since the effects of the turbulence can be isolated from other disturbances of the flow.

In this paper, a DNS study on the effect of TFS on the transition-in-wake regime of a circular cylinder is presented. The aim of the study is to determine if and how the transition with TFS differs from a transition with LFS. The entire transition-in-wake regime is considered, by using $120 \leq \mathrm{Re} \leq 350$. The structure of the paper is the following: in Section 2, the framework and validation of the numerical simulations are described. Section 3 is a presentation of the main results, with the discussion split into the different Reynolds number

spans where effects from the TFS are seen. In Section 4, TFS flows with different turbulence properties (intensity, scale and length of the turbulence production domain) are considered, before conclusions are drawn in Section 5.

2. Methodology

To perform the simulations, the high-order finite-difference code for compressible hydrodynamic flows known as The Pencil Code (see [19,20]) has been used. The governing equations of the flow are the continuity equation:

$$\frac{\mathrm{D}\rho}{\mathrm{D}t} = -\rho \boldsymbol{\nabla} \cdot \boldsymbol{u}\,, \tag{1}$$

and the momentum equation:

$$\rho \frac{\mathrm{D}\boldsymbol{u}}{\mathrm{D}t} = -\boldsymbol{\nabla} p + \boldsymbol{\nabla} \cdot (2\mu \boldsymbol{S})\ , \tag{2}$$

where ρ, t, $\boldsymbol{u}$ and p are the density, time, velocity vector and pressure, respectively. The rate of strain tensor is given by

$$\boldsymbol{S} = \frac{1}{2}\left(\boldsymbol{\nabla}\boldsymbol{u} + (\boldsymbol{\nabla}\boldsymbol{u})^T\right) - \boldsymbol{I}\left(\frac{1}{3}\boldsymbol{\nabla} \cdot \boldsymbol{u}\right), \tag{3}$$

where $\boldsymbol{I}$ is the identity matrix. The pressure is computed by the ideal gas law, $p = c_s^2 \rho$, where c_s is the speed of sound. The flow is isothermal and weakly compressible (the Mach number is 0.1 in all simulations).

2.1. Numerical method

The equations are discretised with sixth-order central-differences in space and a third-order Runge–Kutta scheme in time. An equidistant Cartesian mesh is used to simplify the process of inserting turbulence upstream of the circular cylinder. The cylinder is situated in the centre of the flow domain (details in Section 2.3), and an immersed boundary method is used to resolve the cylinder boundary.

The immersed boundary method, introduced by Peskin in the 1970s to model flow around heart valves [21], is a class of methods that represent a boundary immersed in a flow with non-body conformal grids (see review article by Mittal and Iaccarino [22] and references therein). As the grid does not conform to the solid boundary, incorporating the boundary conditions requires a modification of the governing equations in the vicinity of the boundary. In our implementation, a discrete forcing approach is used, in which the boundary conditions at the cylinder are enforced through ghost points inside the cylinder. The advantage of this approach is that it allows direct control over the numerical accuracy, stability and discrete conservation properties of the solver.

The seven-point finite-difference stencil used for the sixth-order method is not altered near the surface. Rather, a three-point deep ghost point zone is constructed inside the

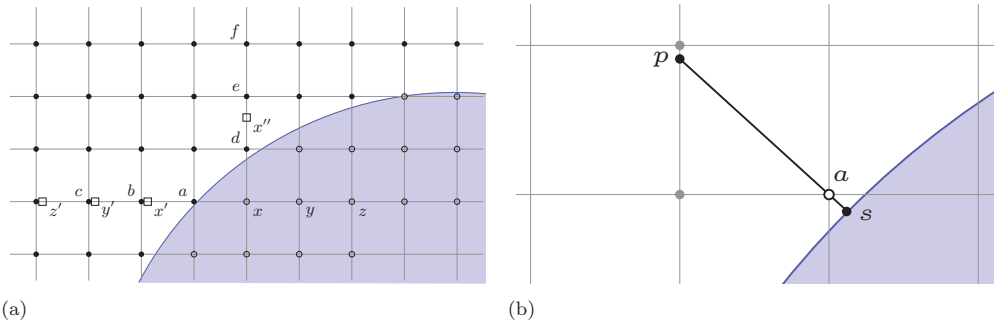

Figure 1. Immersed boundary method. Ghost points (x, y, z; ○) used in the central-difference stencils of fluid points (a–c; ●) are set by mirror points (x', y', z'; □). The mirror points are interpolated along grid lines. When (x; ○) is used to compute vertical velocity components of fluid points (d–f; ●) the corresponding mirror point is (x''; □). For a fluid point (a; ○) very close to the cylinder surface, interpolation between a surface point (s; ●) and the intersection between the surface normal and the first grid line at (p; ●) is used. (a) Ghost and mirror points for velocity computation; (b) special handling of fluid points close to the surface.

solid geometry (unlike the more common single ghost point discretisation, see, e.g. [23]). To resolve the boundary conditions set at the cylinder surface, the ghost points are assigned values from corresponding mirror points. These are no-slip and impermeability for the velocity, and zero gradient in the radial direction for the density. The latter condition can be derived from the ideal gas law and the boundary layer approximation $\left(\frac{\partial p}{\partial n} = 0, \text{ where } n \text{ is the wall normal direction}\right)$ for an isothermal flow.

Ghost points and mirror points used for velocity are computed along Cartesian grid lines; see Figure 1(a). Note that ghost point x is set by mirror point x' when used to compute the horizontal velocity component at fluid points a–c, and by mirror point x'' when used to compute the vertical velocity component at fluid points d–f. Ghost points used to resolve the density gradient are set from mirror points in the radial direction, since only the radial gradient is known (details in [24]). Computation along radial lines minimises the distance between a ghost point and its corresponding mirror point. The use of mirror points along grid lines, however, ensures that the mirror points are closer to the fluid points where the corresponding ghost points are used in the finite-difference stencils. This has been found advantageous, as spurious effects that arise due to the effective delocalised dependency in the finite-differences are reduced. Further, interpolation along grid lines is cheap and implementation of higher-order Lagrangian interpolation is trivial. Here, quadratic interpolation is used along the grid lines. The point where a grid line intersects the surface is always included in an interpolation stencil, thus extrapolation is avoided. Tri-linear interpolation is used to compute the density mirror points.

Special handling is used for fluid points very close to the solid surface: if a fluid point is closer to the surface than some predefined cut-off (e.g. $0.7\Delta x$), a value is explicitly assigned to the fluid point based on an interpolation along the surface normal, as shown in Figure 1(b). The fluid point a is computed by linear interpolation of the values at the surface point s and at the grid intersection point p. The intersection point p is itself interpolated from its nearest neighbours along the grid line.

Table 1. Comparison of mean drag coefficient C_D and Strouhal number St for a range of resolutions and Reynolds numbers for a two-dimensional domain with $L_x = 10D$ and $L_y = 20D$.

	Re = 100		Re = 200		Re = 300		Re = 350	
Resolution	C_D	St	C_D	St	C_D	St	C_D	St
160 × 320	1.49	0.174	1.48	0.204	1.53	0.218	1.55	0.223
240 × 480	1.49	0.176	1.46	0.206	1.46	0.206	1.52	0.225
320 × 640	1.46	0.176	1.42	0.206	1.44	0.220	1.45	0.225
400 × 800	1.47	0.176	1.43	0.205	1.46	0.220	1.47	0.224
480 × 960	1.47	0.176	1.43	0.205	1.45	0.219	1.46	0.224
640 × 1280	1.46	0.176	1.43	0.205	1.46	0.219	1.47	0.224
800 × 1600	1.46	0.176	1.43	0.205	1.46	0.219	1.47	0.223

2.2. Grid resolution

Grid refinement has been performed to determine the necessary resolution to capture the flow phenomena in the transition-in-wake. The number of equidistant grid points on a two-dimensional flow domain with dimensions $L_x \times L_y = 10D \times 20D$ was varied from 160×320 to 800×1600 for Reynolds numbers from 100 to 350. The inflow velocity and cylinder diameter were held constant, while the viscosity was used as a control parameter to set the Reynolds number.

From the grid refinement study, a resolution of $D/\Delta x = D/\Delta y = 40$ (i.e. a 400×800 grid) is found to be sufficient for Reynolds numbers spanning the transition-in-wake state of the flow (see Table 1). For simplicity, the same resolution is used for all Reynolds numbers, although a coarser grid would be sufficient at the lower Reynolds numbers. The laminar boundary layer around the cylinder is thinnest at the front stagnation point. This (non-dimensional) boundary layer thickness is $\tilde{\delta} = \delta/D = 2.4\sqrt{\nu/(BD^2)}$, where $B \approx 4\bar{U}/D$ for weakly compressible flows [25]. Hence, with dimensionless grid spacing $\Delta\tilde{x} = \Delta\tilde{y} = 0.025$, the boundary layer is at minimum 4.8 grid points deep for $\mathrm{Re} = 100$ ($\tilde{\delta} = 0.12$) and 2.6 grid points deep for $\mathrm{Re} = 350$ ($\tilde{\delta} = 0.064$). In practice, this guarantees that at most one of the grid points used for interpolation of the mirror point farthest from the surface (z' in Figure 1(a)) is (barely) outside the boundary layer for $\mathrm{Re} = 350$. All other interpolation grid points, and all mirror points, are guaranteed to be inside the boundary layer at this resolution. This is due to the special handling of grid points closer to the surface than $0.7\Delta x$, ensuring that a ghost point is not used if it is farther than $2.3\Delta x$ from the surface.

The stability requirement for the Runge–Kutta method for a weakly compressible flow imposes a very strict limit on the time step. An adaptable time step is used, which results in the dimensionless time step $\Delta\tilde{t} = \Delta t\bar{U}/D \leq 1.3 \times 10^{-3}$ after the development of the von Kármán vortex street. To verify that this time step is adequate, two-dimensional flow simulations were performed on the 400×800 grid, with fixed time stepping. Reducing the time step to $\Delta\tilde{t} \leq 1.0 \times 10^{-4}$ had a negligible impact on the flow simulation, increasing C_D and St only by 0.015% and 0.06%, respectively.

For DNS, it is not sufficient to resolve the boundary layer around the cylinder, all scales of the TFS (spatial and temporal) must also be resolved. Fortunately, at the low to moderate Reynolds numbers spanning the transition-in-wake regime, the Kolmogorov length scale $\eta = (\nu^3/\varepsilon)^{1/4}$, where ε is the average energy dissipation rate, is larger than the necessary resolution required to resolve the boundary layer, for the turbulence considered in this research. The Kolmogorov time scale, $\tau_\eta = (\nu/\varepsilon)^{1/2}$, is substantially larger than the

Table 2. Comparison of the Kolmogorov microscales with spatial and temporal resolution for the TFS with integral scale $\Lambda/D \approx 1$ for $\mathrm{Re} = 100$ and $\mathrm{Re} = 350$. Non-dimensional properties given by $\tilde{\varepsilon} = \varepsilon D/\bar{U}^3$, $\tilde{\eta} = \eta/D$, $\tilde{\tau}_\eta = \tau_\eta \bar{U}/D$. The grid is equidistant with $\Delta x = \Delta y$.

Re	$\tilde{\varepsilon}_{\max}$	$\tilde{\eta}$	$\tilde{\tau}_\eta$	$\eta/\Delta x$	$\tau_\eta/\Delta t$
100	0.0161	0.089	0.788	3.55	606
350	0.0116	0.038	0.497	1.51	382

required temporal resolution imposed by the stability requirement (details are found in Table 2).

2.3. Computational domain

The computational domain consists of two rectangular boxes. In the first box, isotropic turbulence is generated by external forcing on given wave numbers (details in [26]). This domain (left box in Figure 2, henceforth called the turbulence domain) has periodic boundary conditions in all directions and is equal in size to the flow domain (more on this in Section 4.3). Once the forced turbulence is statistically stationary, slices of flow quantities from the turbulence domain are added to the inlet of the flow domain (right box in Figure 2). The flow domain has mean inlet velocity $\bar{\mathbf{U}} = (\bar{U}, 0, 0)$. Since the mean velocity in the turbulent box is zero, this mean inlet velocity is not affected by the added turbulent velocities. Hence, the inlet velocity is $\mathbf{U} = \bar{\mathbf{U}} + \mathbf{u}'$, where $\mathbf{u}'$ is updated at every time step using data from the turbulence domain. To avoid outflows at the inlet, the turbulence intensity is limited such that $\max |u_x'| \leq \bar{U}$. Navier–Stokes characteristic boundary conditions, which is a formulation that uses one-dimensional characteristic wave relations to allow acoustic waves to pass through the boundaries, are used both at the inlet and at the outlet of the flow domain [27]. The boundaries normal to the mean flow direction are periodic.

The size of the flow domain is $(L_x, L_y, L_z) = (12D, 6D, 8D)$. The size of the domain is chosen to be sufficiently large to resolve the flow phenomena qualitatively. Consider the

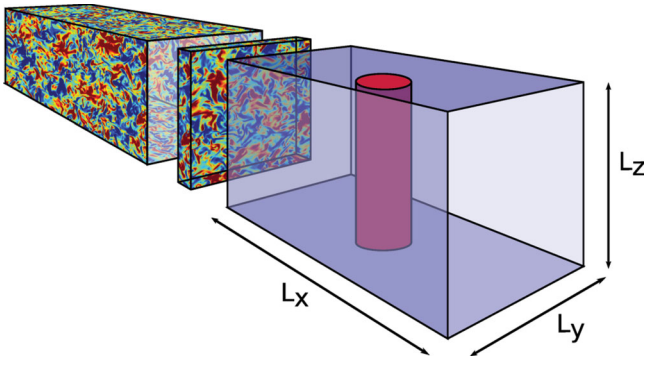

Figure 2. Computational domain, split into two rectangular boxes. Left box for turbulence generation and right box for flow domain. Thin slices of velocity data are taken from the turbulence domain and added to the velocity on the inlet of the flow domain, illustrated here by a thin rectangular box between the two domains. The slice thickness and cylinder diameter are not to scale.

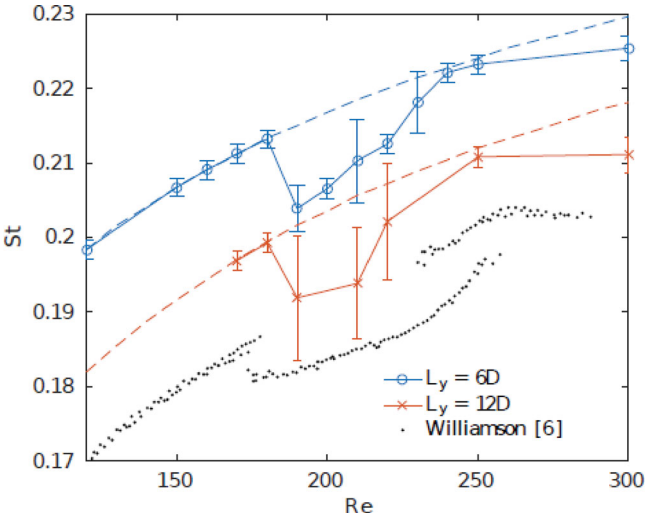

Figure 3. Comparison of St–Re relationships for flows with laminar free-stream conditions, for Reynolds numbers spanning over the transition-in-wake regime. $L_y = 6D$: -o- 3D, _ _ 2D; $L_y = 12D$: -x- 3D, _ _ 2D; • data from experiments by Williamson [6].

solid blue curve with o-markers in Figure 3, depicting the Strouhal number as a function of Reynolds number for the flow in the transitional regime with LFS. The results are compared with experimental results from Williamson [6] (black dots). Results from two-dimensional simulations, where the transition-in-wake does not occur, are also included in the figure (dashed blue line). The qualitative match between the three-dimensional simulations and the experimental results is good, but the quantitative match is poor. A discrepancy between the oblique vortex shedding results by Williamson [6] and the parallel vortex shedding from the DNS is expected, as parallel vortices are shed at a somewhat higher frequency than oblique vortices (see [28]). The mismatch between the experimental and DNS results is, however, too large to be attributed to this effect alone. It is well known that a limited L_y will generate blockage effects in the flow [29,30]. Previous validation runs show that L_y is the domain size parameter that has the greatest influence on the computed Strouhal number [31]. The blockage ratio is $D/L_y = 0.167$, and significantly larger St values are found in the simulations than in the experimental data. The blockage effect, however, does not affect the value of Re_c or the increase in St in the upper Re part of the transition. Doubling L_y, from $6D$ to $12D$, and thus approaching the recommended distance of $8D$ from the lateral boundaries to the cylinder, as suggested by Behr et al. [29], reduces the St values by ≈9% (red curve with x-markers in Figure 3). Since the quantitative value of St is not of interest to us, $L_y = 6D$ is used in the subsequent simulations in order to keep the computational costs manageable. Similarly to Thompson et al. [32], we believe that the restricted domain does not alter the essential physics underlying the development and interaction of the three-dimensional structures. Note that even with this limited domain width, the typical cost of running a simulation resulting in a single point in Figure 3 is 5.4×10^3 CPU hours. For simulations with TFS the typical simulation time is approximately 40% longer.

Two-dimensional simulations with varying upstream and downstream lengths have been performed, and the results showed that a cylinder situated in the centre of a $12D$ long

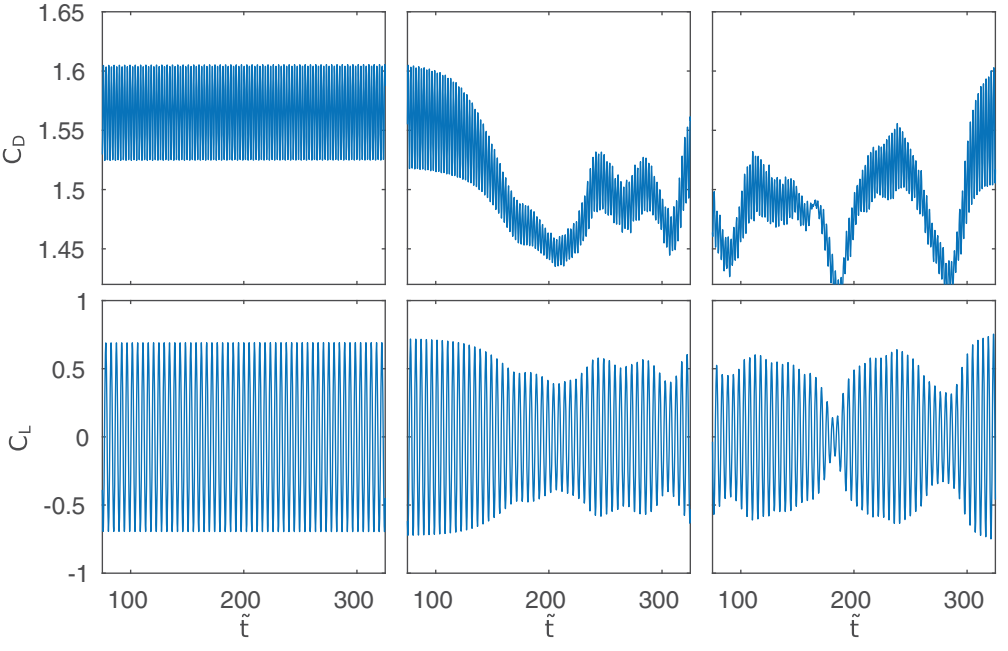

Figure 4. The computed instantaneous drag and lift coefficients, C_D and C_L, respectively, for Reynolds numbers 180 (left), 190 (middle) and 210 (right) as a function of the dimensionless time $\tilde{t} = t\bar{U}/D$.

flow domain gives accurate results for the shedding frequency. The simulations were performed for Re = 100, with upstream and downstream lengths varied up to $50D$ each. The Strouhal number St was barely affected by these lengths, as long as the lengths were above a certain threshold. Results from validation runs with $L_x = 20$ and Re spanning over the transition-in-wake region (with the cylinder in the centre of the domain) are not included in Figure 3 since they are indistinguishable from the corresponding results with $L_x = 12D$.

The spanwise length L_z is chosen sufficiently large to allow room for at least two wavelengths of the mode A instabilities inside the flow domain at Re_c. The choice of the spanwise length is based on the findings of Posdziech and Grundmann [11], that an L_z twice as large as the most unstable wavelength of the mode A instabilities ($\lambda_A \lesssim 4D$) guarantees an accurate reproduction of the measurements.

2.4. Measuring the shedding frequency

There is a large variation in the size of the error bars in Figure 3. This stems from the nature of the shedding of vortices in the transitional regime, particularly for Reynolds numbers where several vortex dislocations occur.

Let us consider as an illustration Figure 4, depicting the drag and lift coefficients for Re = 180, 190 and 210. For the two-dimensional vortex shedding (Re = 180) the coefficients vary sinusoidally with a constant shedding frequency. For $\mathrm{Re} > \mathrm{Re}_c$, the oscillations diverge from a sinusoidal behaviour. The sharpest amplitude drops in the drag and lift coefficients correspond to time instants where vortex dislocations develop in the cylinder wake.

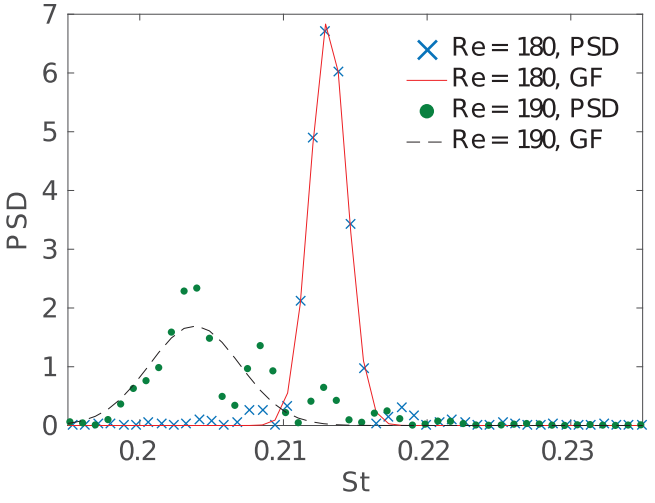

Figure 5. Power spectral density (PSD) as a function of Strouhal number with curve fitted Gaussian distribution (GF), for LFS flow at Re = 180 (PSD:×, GF:—) and Re = 190 (PSD:●, GF:- - -).

The vortex dislocations also affect the vortex shedding frequency, i.e. strong intermittent vortex dislocations result in a drop in St over a short time interval.

To find the shedding frequency from the lift data, a Lomb–Scargle power spectral density (PSD) estimate [33] is computed, followed by a Gaussian curve fitting. The Lomb–Scargle periodogram is preferred rather than a Fourier transform, due to uneven time sampling from the adaptable time step in the simulations. A curve fitting in frequency space is necessary since the Strouhal number varies with time in the transitional regime (particularly in regions with intermittent vortex dislocations). A Gaussian fit is used since the strongest peaks in frequency space generate a normal-like distribution (admittedly skewed for $\mathrm{Re} > \mathrm{Re}_c$); see Figure 5. The error bars in the St–Re curves in Figures 3, 6, 7, 8 and 9 are standard deviations of the curve-fitted Gaussian distributions in frequency space. Although using a moving average over extrema would suffice for computing St in the LFS simulations, for flow with a TFS high-frequency noise from the turbulence makes measurements of shedding frequency without the transformation to frequency space hard and inaccurate. Another advantage of the Gaussian fitting (compared to, e.g. setting St equal to the dominant frequency of the PSD) is that the standard deviation of the fitted curve provides information about the St span at each Re. In particular, this brings attention to simulations that develop vortex shedding that alternates between two- and three-dimensional vortex shedding. These quasi-stable states (see Section 4) are easily overlooked by using the dominating shedding frequency directly.

The simulations are run for 50–120 shedding periods after the vortex shedding has developed. The simulations in which the strongest vortex dislocations appear are run for the longest time to avoid an incorrect influence of the dislocations on St. Imagine, for instance, that only 30 periods were included for Re = 210, i.e. terminating the simulation at $\tilde{t}$ between 200 and 250. This would give an excessive influence of the strong vortex dislocation close to $\tilde{t} = 200$ on the flow statistics. For all but a few simulations, the flow is considered to be developed after a time corresponding to approximately 20 shedding periods. The

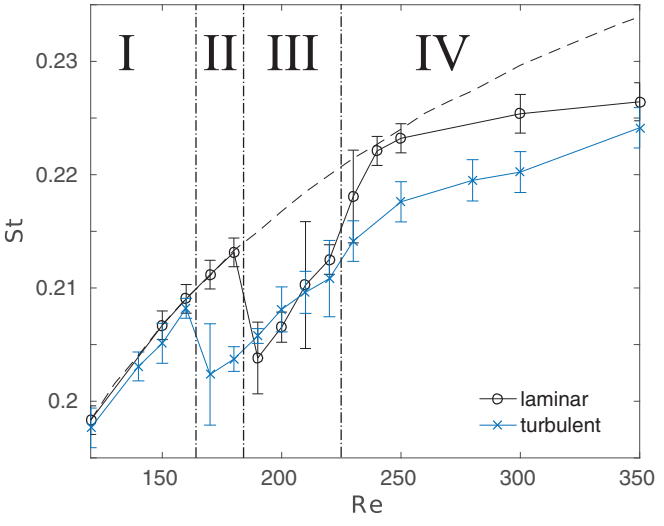

Figure 6. Comparison of St–Re relationships for flows with and without free-stream turbulence introduced upstream of the cylinder, for Reynolds numbers spanning over the transition-in-wake regime: -o- LFS; -x- TFS; - - 2D LFS.

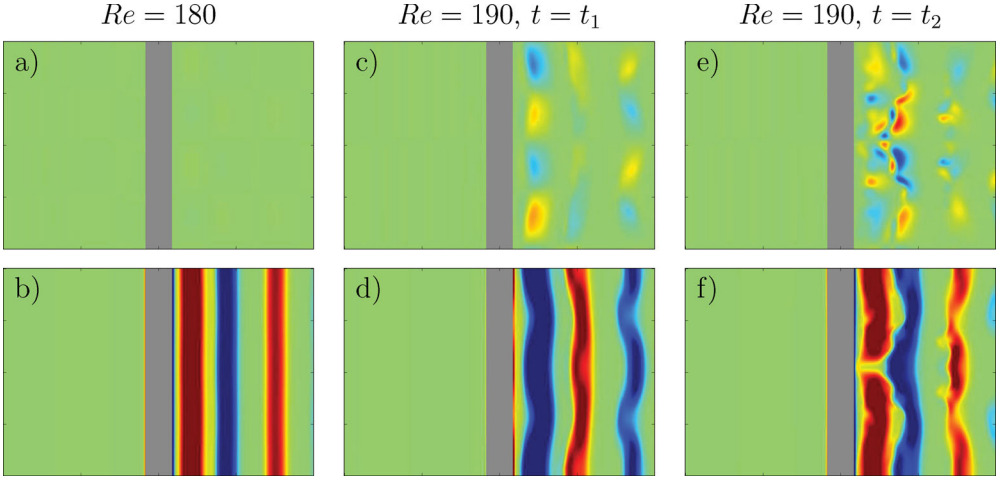

Figure 7. Laminar free-stream. Contours of instantaneous vorticity ω_y (top) and ω_z (bottom) in a plane along the streamwise direction, through the cylinder axis, plotted for Re = 180 (left) and Re = 190 (middle and right). Top and bottom frames correspond to the same time instant. Contour plots for two time instants are given for Re = 190: t_1, time instant without vortex dislocation; t_2, time instant with vortex dislocation.

exceptions are for Re very close to the critical Reynolds number, where the flow needs longer time to develop before the measurements start.

3. Effects of high-intensity free-stream turbulence on the transition-in-wake

Turbulence with intensity $T_i = 25\%$ and integral scale $\Lambda = D$ is inserted at the inlet of the flow domain for simulations with Reynolds numbers ranging from 120 to 350. The

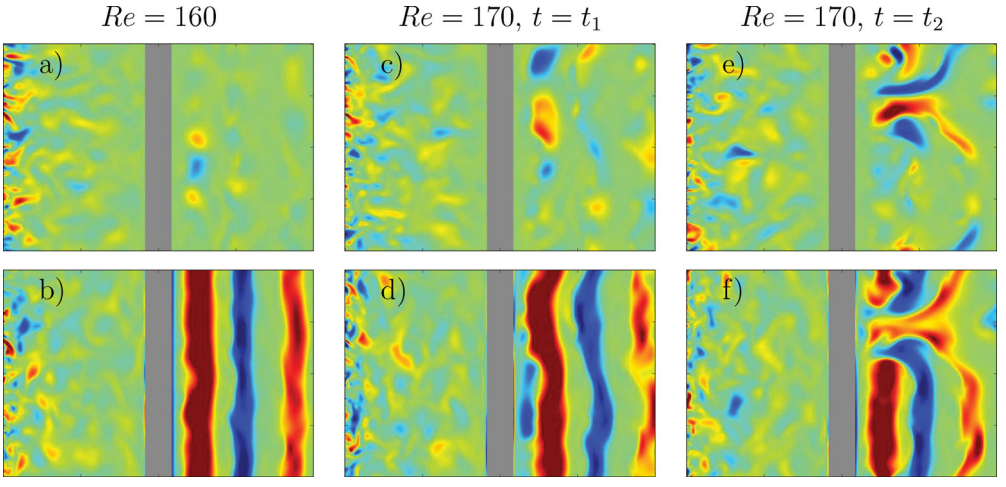

Figure 8. Turbulent free-stream. Contours of instantaneous vorticity ω_y(top) and ω_z (bottom) in a plane along the streamwise direction, through the cylinder axis, plotted for Re = 160 (left) and Re = 170 (middle and right). Top and bottom frames correspond to the same time instant. Contour plots for two time instants are given for Re = 170: t_1, time instant with vortex dislocation beginning to develop; t_2, time instant with fully developed vortex dislocation.

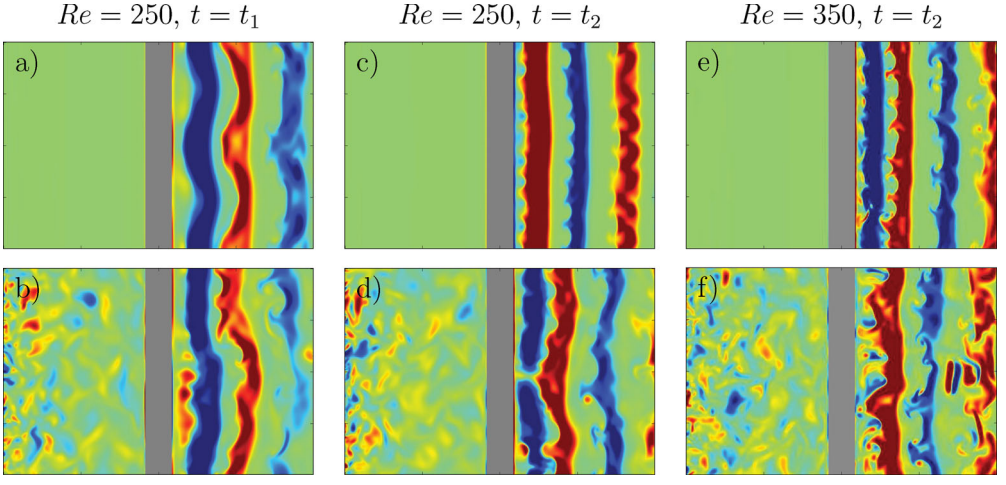

Figure 9. Contours of instantaneous vorticity ω_z in a plane along the streamwise direction, through the cylinder axis, plotted for Re = 250 (left and middle) and Re = 350 (right) for flow simulations with LFS (top) and TFS (bottom). Contour plots for two time instants are given for Re = 250, t_1, early development of instabilities; t_2, asymptotic state ($t_2 \gg t_1$). Only the asymptotic state is shown for Re = 350.

high intensity turbulence decays in the flow direction, and reaches the cylinder surface with an intensity of 10.5%–13.5% (highest decay of T_i for the lowest flow Re). Figure 6 depicts the resulting St–Re relationship, together with results from the LFS simulations. For the lowest and intermediate Re, corresponding to Regions I and III in the figure, the difference between St for the two cases is negligible. In Regions II and IV, this is not the case.

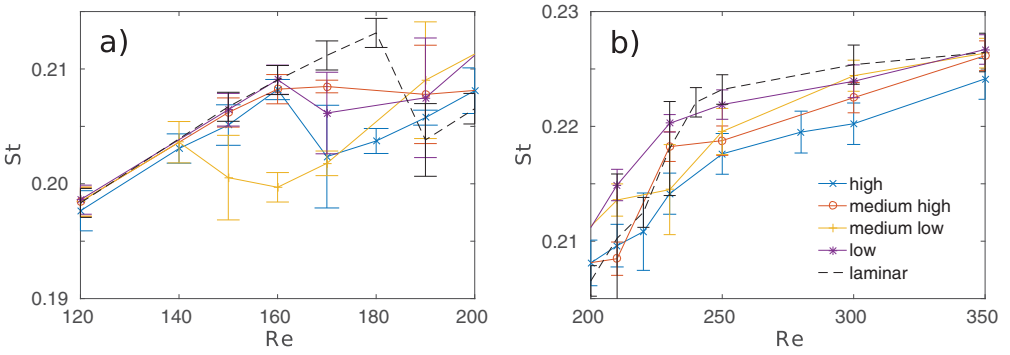

Figure 10. Comparison of St–Re relationships for flows with TFS with different turbulence intensities T_i on the inlet of the flow domain: -x- 25%; -o- 13.5%; -+- 8.1%; -*- 4.8%; - - LFS.

In this section, we will discuss the two regions where the TFS and LFS results differ, before considering the effect of varying the properties of the TFS (intensity, scale and length of the turbulence domain) in Section 4.

3.1. Mode A instabilities and the onset of three-dimensionality in the wake

The drop in shedding frequency at the onset of three-dimensionality in the wake is known to be closely related to the mode *A* instabilities and vortex dislocations in the wake of the cylinder for flows with LFS conditions. This is confirmed in our simulations by looking at instantaneous plots of the vorticity ($\vec{\omega} = \nabla \times \vec{u}$) in a plane along the flow direction and the cylinder axis (the *xz*-plane).

The wake at Re = 180 is purely two-dimensional, as seen by the lack of cross-stream vorticity in Figure 10(a). At Re = 190, mode *A* instabilities (with $\lambda_A \approx 4D$) have developed in the wake; see Figure 10(c–f). A vortex dislocation is seen in Figure 10(e,f), obscuring the observations of mode *A* instabilities.

The drop in St occurs at lower Re for the TFS simulations as compared to the LFS, hence, $\mathrm{Re}_{c,\,\mathrm{TFS}} < \mathrm{Re}_c$ (see Region II of Figure 6). Based on the results with LFS, one would expect this to be due to mode *A* instabilities with vortex dislocations occurring at lower Reynolds numbers as a result of the TFS in the flow. Figure 11 shows instantaneous contours for the TFS flow in Region II and confirms this to some degree: The inherent three-dimensionality in the TFS results in three-dimensional flow effects even at $\mathrm{Re} < \mathrm{Re}_{c,\,\mathrm{TFS}}$, distorting the vorticity plots. This is apparent as $\omega_y \neq 0$ in the near wake in Figure 11(a) although St has not dropped from the two-dimensional mode (Re = 160 data point in Figure 6). Despite this 'noise', coherent flow structures can be observed in the contour plots. Let us compare Figure 11(c,d) to Figure 10(c,d), depicting ω_y and ω_z for TFS flow with $\mathrm{Re} > \mathrm{Re}_{c,\,\mathrm{TFS}}$ and LFS flow with $\mathrm{Re} > \mathrm{Re}_c$, respectively. Vortex dislocations do not dominate the near wake at the specific time instant of these snapshots. While a mode *A* instability is clearly visible in the LFS contours, this mode is less clear in the TFS case. There is an alternation between positive and negative ω_y in Figure 11(c), similar to the variation in the LFS flow, and the wavy structures in Figure 11(d) appear to have a wavelength close to 4*D*. The mode *A*

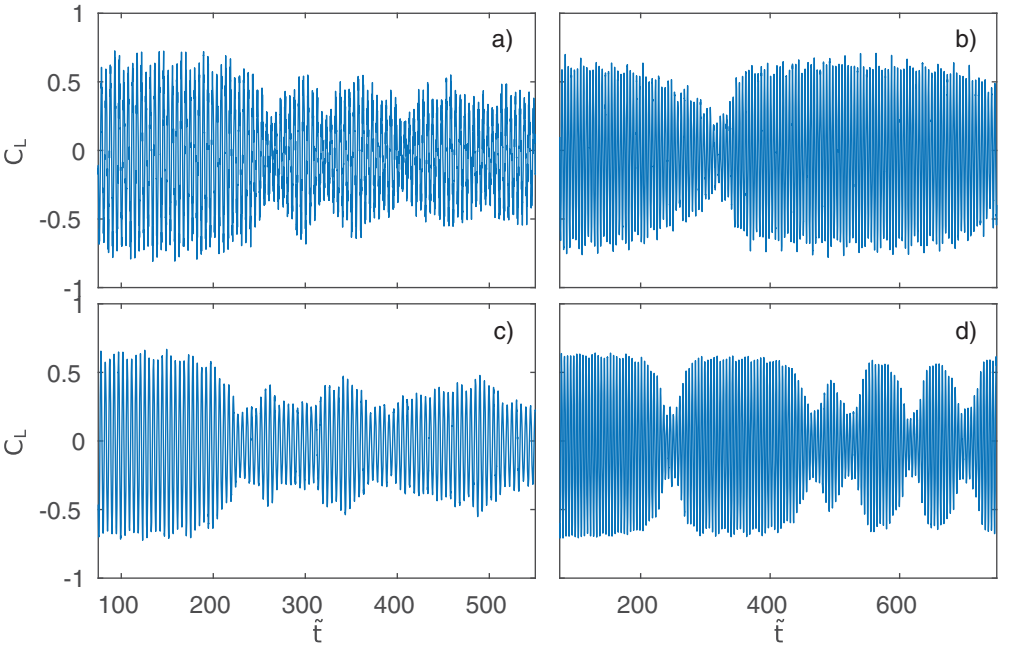

Figure 11. Instantaneous lift coefficient C_L of the cylinder as a function of the dimensionless time $\tilde{t} = t\bar{U}/D$, for flows with Re = 170 and free-stream turbulence upstream of the cylinder. The intensity T_i of the turbulence at the inlet of the flow domain is: (a) 25%; (b) 13.5%; (c) 8.1%; (d) 4.8%.

instability is present, but the view is obscured by a vortex dislocation beginning to develop in the upper half of the frames.

Strong vortex dislocations develop at Re = 170, as can be seen in Figure 11(e,f). The pattern is similar to the experimental flow visualisation by Zhang et al. (see [9], Figure 5), where the term vortex adhesion is used to describe this phenomenon. The development in time, from Figure 11(d–f), appears to be the development of a large-scale structure, and similar vortex dislocation patterns occur repeatedly after the initialisation of the simulation for this Re. The snapshot in Figure 11(f) is among the clearest observations of a vortex dislocation appearing to adhere to the cylinder at this Reynolds number.

Henderson [10] reported that spot-like disturbances (i.e. vortex dislocations) always developed from small perturbations at sufficiently large $\mathrm{Re} > \mathrm{Re}_c$ and $L_z > \lambda_A$, and that these large-scale structures only appear in a natural transition after mode *A* instability. The results of the present study can hardly be considered as a natural transition, as the TFS acts as a strong perturbation on the wake instability; the shift of the critical Reynolds number to a lower value is a direct consequence of the TFS. Yet, similar to the observations by Henderson [10], the vortex dislocations in the wake first occur for $\mathrm{Re} > \mathrm{Re}_{c,\,\mathrm{TFS}}$. The strong vortex dislocation and inherent three-dimensionality of the TFS obscure the view of mode *A* instability in the flow. Still, the similarity between the drop in St in Region II of Figure 6 for the two flow cases, the presence of vortex dislocations in Figure 11(e,f) and the vorticity snapshot in Figure 11(d), are strong indications of the existence of mode *A* instabilities at Re = 170 for the TFS flow past the cylinder.

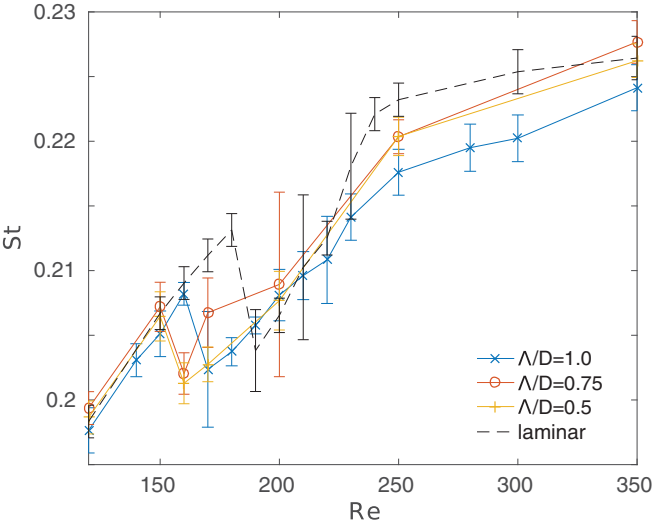

Figure 12. Comparison of St–Re relationships for flows with TFS with $T_i = 25\%$ and different integral scales: -x- $\Lambda/D = 1.0$; -o- $\Lambda/D = 0.75$; -+- $\Lambda/D = 0.5$; - - LFS.

3.2. Mixed instability modes in the upper part of the transition

In moving from Region III to Region IV of Figure 6 the results for TFS and LFS diverge. The difference in shedding frequency between the two cases remains almost constant for $250 \leq \mathrm{Re} \leq 300$, before decreasing somewhat for $\mathrm{Re} = 350$.

The detailed analysis by Henderson [10] revealed a spatio-temporal chaos in the transition to a wake dominated by mode *B* instabilities at $\mathrm{Re} = 265$. Since mode *B* instabilities are slower to develop than mode *A* instabilities (in development of the mode *B* dominated near wake) there exists a temporal region dominated by mode *A* instabilities and a temporal region of mixed mode *A* and *B* instabilities even at Re above the threshold where mode *B* is dominant. During this development the shedding frequency is reduced by $\Delta f \in (-0.004, -0.014)$ (corresponding to $\Delta\mathrm{St} \in (-0.04, -0.14)$) as compared to the frequency for the 2D shedding state (see [10], Figure 12).

Figure 12 depicts snapshots of spanwise vorticity ω_z in the central *xz*-plane, with and without TFS, at two different Reynolds numbers in Region IV. The snapshots are taken at times that show the early development of the wake (Figure 12(a,b)) and at times where the wake has had time to reach an asymptotic state (Figure 12(c,f)). After a temporal region of mode *A* dominated flow (Figure 12(a)), the mode *B* dominated near wake develops for the LFS flow. At $t_2 \gg t_1$ the mode *B* instability is clearly visible, with a spanwise wavelength of approximately $1D$ (see Figure 12(c,e)). The spatio-temporal chaos [10] is present in the development of mode *B* instabilities, but comes to an end as the wake settles in a state dominated by mode *B* instabilities. For the flow with TFS mode *B* instabilities have barely started to develop at $\mathrm{Re} = 250$. The vorticity in the near wake (Figure 12(d)) reveals that the flow is more similar to that at the onset of the transition (Figure 11(d)) than with the flow with LFS at $\mathrm{Re} = 250$. Thus, the mode *A* dominated state at t_1 (Figure 12(b)) is not temporal when the free-stream is turbulent. At $\mathrm{Re} = 350$, smaller scale instabilities have developed, with vortex fingers that adhere strongly to the cylinder before the vortices are

distorted and dissipate downstream; see Figure 12(f). The flow is more similar to the LFS case at this Re, although larger-scale disturbances are still present in the near wake.

From the vorticity plots and the reduced shedding frequency, it is evident that the disturbances from the TFS suppress the transition to a near-wake dominated by mode *B* instabilities. The asymptotic state with no discernible large-scale pattern reported by Henderson [10] is not reached with a high-intensity TFS. Rather, the TFS stimulates the existence of mode *A* instabilities, resulting in the mixed state of mode *A* and *B* instabilities at higher Re when the free-stream is turbulent than when it is laminar.

Williamson [7] discussed measurements by Prasad and Williamson [34], where manipulation of the end conditions in experiments made vortex dislocations at $\mathrm{Re} > 260$ possible. By means of this disturbance, the jump to higher St in Region IV of Figure 6 did not occur. A low frequency curve, similar to our TFS results, is shown for Re up to 400 in Williamson [7]. This instability state was called B^* instabilities, where the asterisk denotes vortex dislocations in the flow. It is likely that end conditions might have a similar effect as the TFS, and that the B^* instabilities reported by Williamson [7] are the mixed *A*–*B* instabilities we observe in the present study. Hence, the asterisk denoting vortex dislocations is somewhat misleading. Dislocations are a product of interacting self-exiting mode *A* instabilities, present due to disturbances in the flow, and not unrelated to the flow instabilities and simply forced by end conditions.

4. Effects of varying free-stream turbulence properties on the transition-in-wake

So far, the turbulence inserted at the inlet of the flow domain has been of high intensity and with the integral scale equal to the cylinder diameter. The turbulence has been generated in a turbulence domain equal in length to the flow domain. In this section, we shall consider the effect (if any) that varying these properties of the TFS has on the St–Re relationship in the transition-in-wake state of the flow.

4.1. The effect of the intensity of the TFS

Figure 7 depicts the development of St for a span of Re for flows with TFS with four different turbulence intensities: $T_i = 25\%$, 13.5%, 8.1% and 4.8%, henceforth denoted high, medium high, medium low and low turbulence intensity. At $\mathrm{Re} = 200$, the turbulence intensity decays to 12.2%, 7.4%, 5.2% and 3.6%, respectively, before reaching the cylinder. Lower Re gives a more rapid decay, e.g. the high intensity turbulence ($T_i = 25\%$) decays to 11.1% for $\mathrm{Re} = 150$ and 13.5% for $\mathrm{Re} = 350$, before reaching the cylinder surface.

Consider first the upper part of the St–Re relationship for varying T_i, as seen in Figure 7(b). The effect of the turbulence intensity in the part of the transition-in-wake, where the role of mode *B* instabilities becomes important, is perhaps what one intuitively would expect: A lower T_i yields a St–Re relationship that is more similar to what is found for LFS in the range $250 \leq \mathrm{Re} \leq 350$. The correlation between T_i and St can be understood in light of our discussion in Section 3.2. The TFS stimulates the mode *A* instabilities in the mixed *A*–*B* instability mode (inhibiting the development of pure mode *B* in the near wake). The larger the effect of the mode *A* instabilities, the lower the shedding frequency.

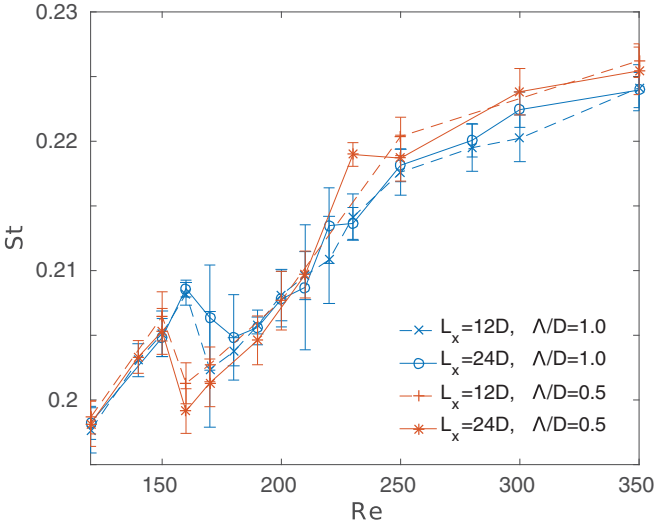

Figure 13. Comparison of St–Re relationships for flows with TFS, with turbulence generated in domains of different size and with different integral scales. Dashed lines for $L_{xT} = 12D$ and solid lines for $L_{xT} = 24D$.

While the high intensity TFS in Section 3 almost completely suppresses the mode *B* instabilities, the results for moderate T_i reflect a more even mix between the two modes for Re = 250 and a wake dominated by mode *B* instabilities for Re = 350.

Consider now the more complex situation at the onset of three-dimensionality in the wake, seen in Figure 7(a). At Re = 170, all TFS simulations have St below the LFS flow (which is two-dimensional for this Reynolds number), yet there is a scatter in the TFS data. For the $T_i = 13.5\%$ and $T_i = 4.8\%$ cases, St is surprisingly high, indicating that the wakes have not fully developed to three-dimensional flows. Further, the early drop in St for the case with medium low turbulence intensity contradicts a possible simple correlation between high T_i and low $\mathrm{Re}_{c,\,\mathrm{TFS}}$ for our T_i range. This reflects the complicated nature of the instability in the transition-in-wake state of the flow. To gain insight into the mechanisms in play here, we take a more detailed look at the temporal development of the flow at Re = 170.

Figure 13 depicts the instantaneous lift coefficient of the cylinder at Re = 170 for the four different TFS intensities. For $T_i = 25\%$ and $T_i = 8.1\%$ the transition to a three-dimensional wake happens at $200 < \tilde{t} < 300$, where the amplitude of C_L drops significantly in Figure 13(a,c). The frequency of the oscillations decreases together with the drop in amplitude. A similar drop in C_L also occurs for the $T_i = 13.5\%$ and $T_i = 4.8\%$ cases at $200 < \tilde{t} < 400$, but C_L returns quickly to its previous amplitude; see Figure 13(b,d). This behaviour can be explained in terms of a single vortex dislocation that is unable to saturate the wake in a mode *A* instability state. When the vortex dislocation disperses, the wake resumes two-dimensional vortex shedding. Such a drop also occurs at $\tilde{t} \approx 800$ for the $T_i = 13.5\%$ case, again followed by a rebound to the two-dimensional vortex street. The low-intensity TFS case (Figure 13(d)) shows several short periods of three-dimensionality in the wake for $\tilde{t} > 400$. A saturated state of mode *A* instabilities is not reached, and the wake

alternates between two- and three-dimensional flow. The result of these quasi-stable shedding modes is a St in-between frequencies computed for three-dimensional flows (high and medium low intensity) and the two-dimensional flow (LFS) at Re = 170. The instantaneous shedding frequency varies between a high and a low mode as the wake alternates between two- and three-dimensional states.

The results for varying turbulence intensities suggest that the TFS destabilises the wake when Re is near the critical Reynolds number, resulting in possible alternations between two- and three-dimensional flow. Furthermore, the onset of three-dimensionality at Re = 150 for $T_i = 8.1\%$ and quasi-stable transition at Re = 170 for $T_i = 13.5\%$ and $T_i = 4.8\%$ suggest that $\mathrm{Re}_{c,\,\mathrm{TFS}}$ is not sharply defined when large disturbances are present in the flow. This is in accordance with the discussion by Williamson [3] on scattered Re_c data reported in experiments. In our cases, however, the disturbance is a TFS, not a contamination in the form of vortex dislocations excited by the end conditions in the experiments.

4.2. The effect of the integral scale of the TFS

Figure 8 depicts the St–Re relationship in the transition-in-wake regime for flows with TFS with different integral scales. The turbulence intensity is approximately 25% at the inlet for each case. However, as small-scale turbulence decays significantly faster than large-scale turbulence, the turbulence intensities for the different flow cases are no longer equal when the turbulence reaches the cylinder. For Re = 200, T_i is 12.2%, 7.2% and 6.7% at the front side of the cylinder for the turbulence with $\Lambda/D = 1.0$, $\Lambda/D = 0.75$ and $\Lambda/D = 0.5$, respectively.

The deviations between the St–Re relationships in Figure 8 are similar to those discussed in the previous subsection. Again, the complicated nature of the onset of the transition-in-wake is seen, particularly by considering the case with $\Lambda/D = 0.75$ for low Re. At Re = 160, three-dimensionality has developed in the flow, but at Re = 170 a quasi-stable shedding mode with St alternating between results for large-scale TFS and LFS occurs. The behaviour is a result of interactions of the TFS with the wake. At Re = 160, conditions are favorable for a saturated state of mode *A* dominating the flow, while at Re = 170 they are not. The results show that the quasi-stable state can occur for $\mathrm{Re} > \mathrm{Re}_{c,\,\mathrm{TFS}}$. For very long simulations, we expect that alternation between arbitrarily long periods of two- and three-dimensional flow in the wake will appear in several of the simulations with TFS. At present, we cannot conclude that a flow in a quasi-stable shedding state eventually will end up in a saturated three-dimensional state.

In the upper part of the transition-in-wake regime, the deviation between the curves in Figure 8 is in accordance with the observations in Section 4.1. The low intensity turbulence associated with the shorter integral scales results in a mixed *A*–*B* instability at Re = 250, whereas the wake is dominated by mode *B* instability at Re = 350.

4.3. The effect of the length of the turbulence domain

As described in Section 2.3, slices of forced turbulence from the turbulence domain are inserted on the inlet of the flow domain, from where the inflow turbulence is convected past the cylinder. The validity of introducing turbulence in a flow in such a way has not yet been addressed. Therefore, a short validation section is included here, with a focus on the

effect of the size of the domain used for turbulence generation. The interesting length of the turbulence domain is the length corresponding to the streamwise direction in the flow domain (denoted by L_{xT}). This is the only free length parameter of the turbulence domain (the other lengths must match the size of the flow domain inlet).

Inserting turbulence from slices taken from a rectangular domain into the flow domain will introduce an artificial periodicity. This is because the same turbulence re-enters the inlet several times over the time span that the wake flow is investigated, due to the cycling over slices along L_{xT}. The artificial period introduced is the time it takes to iterate through all the slices along the x-direction in the turbulence domain, i.e. the time between each re-occurrence of the same slice at the inlet of the flow domain. The frequency introduced from the turbulence domain is $f_T = \bar{U}/L_{xT}$. Non-dimensionalising this frequency with the characteristic length (cylinder diameter D) and characteristic velocity in the flow domain yields $\tilde{f}_T = D/L_{xT}$. For a turbulence domain equal in length to the flow domain ($12D$), $\tilde{f}_T = 0.083$, which is close enough to the Strouhal number in the transitional regime to not be neglected prior to further investigations.

Figure 9 depicts results from flow simulations with TFS generated in domains with $L_{xT} = 12D$ and $L_{xT} = 24D$. Turbulence of two different integral scales are included for both domain sizes. Doubling L_{xT} does not affect the general trends in the St–Re relationship, but a deviation occurs for $\mathrm{Re} = 170$ for the cases with $\Lambda/D = 1.0$. The deviation is in the behaviour at Re close to $\mathrm{Re}_{c,\,\mathrm{TFS}}$, discussed in Sections 4.1 and 4.2. Unlike the flow with TFS generated in the $L_{xT} = 12D$ domain, flow from the simulations with $L_{xT} = 24D$ and $\Lambda/D = 1.0$ enters a quasi-stable state, alternating between two- and three-dimensional shedding modes, at $\mathrm{Re} = 170$. The resulting St is therefore in-between the results for TFS and LFS at this Re. This is not an effect related to the artificial periodicity, but rather of a different realisation of the same turbulence having less favourable conditions for a saturated mode A dominated flow for this particular simulation. The effect of the turbulence domain length is negligible.

5. Conclusions

In the DNS presented here, free-stream turbulence has been inserted upstream of a circular cylinder for Reynolds numbers spanning over the entire transition-in-wake state of the flow. Distinct effects of the turbulence on the transition-in-wake are observed in two particular Re regions. These regions (denoted as Regions II and IV in Figure 6) have Re near the onset of three-dimensionality in the flow and Re where mode B instabilities dominate the wake for flows with LFS, respectively.

With TFS, the critical Reynolds number, identified by the sudden drop in shedding frequency due to the three-dimensional flow effects, is not sharply defined. This is not surprising, as the instability at the onset of the transition-in-wake state of the flow is subcritical, hence, disturbances in the flow can shift the point where the transition occurs. The shift due to the TFS is, however, to lower Re than allowed by the hysteresis pattern seen in experiments for the subcritical instability. With TFS, we observe $150 \lesssim \mathrm{Re}_{c,\,\mathrm{TFS}} \lesssim 170$ (as compared to $\mathrm{Re}_c \simeq 190$ for LFS), with intermittent vortex dislocations present in the wake for $\mathrm{Re} > \mathrm{Re}_{c,\,\mathrm{TFS}}$. Quasi-stable shedding states, in which the wake alternates between two- and three-dimensional vortex shedding, are observed in several of our simulations for $\mathrm{Re} \approx$

$Re_{c,\,TFS}$. In such cases, the shedding frequency is reduced when vortex dislocations occur in the wake. The vortex dislocations do not, however, lead to a saturated state of mode *A* instabilities. Rather, the wake either returns to a state of two-dimensional vortex shedding, until the next vortex dislocation occurs, or stays in a three-dimensional shedding state for some time before returning to the two-dimensional state.

Variations of the intensity and integral scale of the TFS revealed the complexity of the onset of the transition-in-wake state of the flow. For turbulence intensity between 3.6% and 12.2%, no correlation between intensity and $Re_{c,\,TFS}$ was found. Surprisingly, the lowest $Re_{c,\,TFS}$ was seen for T_i in-between the two extremes. A reduction of the integral scale of the turbulence resulted in a lower $Re_{c,\,TFS}$. Unfortunately, the integral scale of the turbulence could not be isolated from the intensity as small-scale turbulence decays faster than the large scales in the flow domain. The results are therefore inconclusive in regard to the effect of the integral scale.

In the discussion by Williamson [3] regarding the scatter in Re_c data reported from experiments, Williamson concluded that (in absence of other effects) the scatter can be accounted for by contamination from end conditions. The scatter of the critical Reynolds number in our simulations show another possible source of Re_c variation. The disturbances in the flow from the TFS were large enough to perturb the flow and initiate the transition at a significantly lower Re than for a corresponding flow with LFS and identical end conditions. Hence, in the absence of other effects (including contamination from end conditions), the scatter in Re_c can be ascribed to turbulence in the free-stream.

The second range of Re, in which an effect from the TFS is seen, is the region that for LFS is dominated by mode *B* instabilities. A lower shedding frequency is observed for the simulations with TFS in this region. This is due to the TFS stimulating the existence of mode *A* instabilities, thereby inhibiting the development of a near wake dominated by mode *B* instabilities. Simulations with varying turbulence intensities revealed a correlation between this effect and T_i. A lower T_i means a closer relationship between the TFS flow and the LFS flow for $Re \geq 250$.

The lowest intensity case of our DNS has turbulence with T_i that has decayed to approximately 3% before it reaches the cylinder for $Re \approx Re_c$. An interesting extension of this study would be to find a cut-off for the intensity of the TFS that forces the transition.

Disclosure statement

No potential conflict of interest was reported by the authors.

Funding

We would like to acknowledge that this research has received funding from the Research Council of Norway (Norges Forskningsråd) under the FRINATEK Grant [grant number 231444]. This research was supported in part with computational resources provided by UNINETT Sigma2 AS [project number NN9405K], [project number NN2649K].

ORCID

J. R. Aarnes http://orcid.org/0000-0002-5899-2597

References

[1] Provansal M, Mathis C, Boyer L. Bénard-von Kármán instability: transient and forced regimes. J Fluid Mech. 1987;182:1–22.
[2] Zdravkovich MM. Flow around circular cylinders: volume 1: fundamentals. Oxford (UK): Oxford University Press; 1997.
[3] Williamson CHK. Vortex dynamics in the cylinder wake. Ann Rev Fluid Mech. 1996;28:477–539.
[4] Barkley D, Henderson RD. Three-dimensional Floquet stability analysis of the wake of a circular cylinder. J Fluid Mech. 1996;322:215–241.
[5] Henderson RD, Barkley D. Secondary instability in the wake of a circular cylinder. Phys Fluids. 1996;8:1683–1685.
[6] Williamson CHK. The existence of two stages in the transition to three-dimensionality of a cylinder wake. J Fluid Mech. 1988;31:3165–3168.
[7] Williamson CHK. Three-dimensional wake transition. J Fluid Mech. 1996;328:345–407.
[8] Williamson CHK. The natural and forced formation of spot-like 'vortex dislocations' in the transition of a wake. J Fluid Mech. 1992;243:393–441.
[9] Zhang HQ, Fey U, Noack BR, et al. On the transition of the cylinder wake. Phys Fluids. 1995; 7: 779–794.
[10] Henderson RD. Nonlinear dynamics and pattern formation in turbulent wake transition. J Fluid Mech. 1997;352:65–112.
[11] Posdziech O, Grundmann R. Numerical simulation of the flow around an infinitely long circular cylinder in the transition regime. Theor Comp Fluid Dyn. 2001;15:121–141.
[12] Barkley D, Tuckerman L, Golubitsky M. Bifurcation theory for three-dimensional flow in the wake of a circular cylinder. Phys Rev E. 2000;61:5247–5252.
[13] Gerrard JH. The wakes of cylindrical bluff bodies at low Reynolds number. Phil Trans R Soc A. 1978;288:351–382.
[14] Norberg C. An experimental investigation of the flow around a circular cylinder: influence of aspect ratio. J Fluid Mech. 1994;258:287–316.
[15] Bloor MS. The transition to turbulence in the wake of a circular cylinder. J Fluid Mech. 1964;19:290–304.
[16] Hussain AKMF, Ramjee V. Periodic wake behind a circular cylinder at low Reynolds numbers. Aeronaut Q. 1976;27:123–142.
[17] Zdravkovich MM. Conceptual overview of laminar and turbulent flows past smooth and rough circular cylinders. J Wind Eng Ind Aerodyn. 1990;33:53–62.
[18] Norberg C. Effects of Reynolds number and a low intensity freestream turbulence on the flow around a circular cylinder. Gothenburg, Sweden: Dept. Applied Thermodynamics and Fluid Mechanics, Chalmers University of Technology; 1987. 87/2.
[19] Brandenburg A, Dobler W. Hydromagnetic turbulence in computer simulations. Comput Phys Commun. 2002;147:471–475.
[20] pencil-code.nordita.org [Internet]. Stockholm (SE): NORDITA; [updated 2017 June 12]. Available from: https://github.com/pencil-code
[21] Peskin CS. Flow patterns around heart valves: a numerical method. J Comput Phys. 1972;10:252–271.
[22] Mittal R, Iaccarino G. Immersed boundary methods. Annu Rev Fluid Mech. 2005;37:239–261.
[23] Tseng YH, Ferziger JH. A ghost-cell immersed boundary method for flow in complex geometry. J Comput Phys. 2003;192:593–623.
[24] Haugen NEL, Kragset S. Particle impaction on a cylinder in a crossflow as function of Stokes and Reynolds numbers. J Fluid Mech. 2010;661:239–261.
[25] White FM. Viscous fluid flow. 3rd ed. Boston (MA): McGraw-Hill Higher Education; 2006.
[26] Haugen NEL, Brandenburg A. Hydrodynamic and hydromagnetic energy spectra from large eddy simulations. Phys Fluids. 2006;18:075106.
[27] Poinsot TJ, Lele SK. Boundary conditions for direct simulations of compressible viscous flows. J Comput Phys. 1992;101:104–129.

[28] Williamson CHK. Defining a universal and continuous Strouhal-Reynolds number relationship for the laminar vortex shedding of a circular cylinder. Phys Fluids. 1988;31:2742–2744.
[29] Behr M, Hastreiter D, Mittal S, et al. Incompressible flow past a circular cylinder: dependence of the computed flow field on the location of the lateral boundaries. Comput Methods Appl Mech Eng. 1995; 123: 309–316.
[30] Anagnostopoulos P, Iliadis G, Richardson S. Numerical study of the blockage effects on viscous flow past a circular cylinder. Int J Numer Meth Fluids. 1996;22:1061–1074.
[31] Aarnes JR, Haugen NEL, Andersson HI. On validation and implementation of an immersed boundary method in a high order finite difference code for flow simulations. In: Skallerud B, Andersson HI, editors. MekIt'15: eight national conference on computational mechanics; 2015 May 18–19; Trondheim (Norway). Barcelona (Spain): International Center for Numerical Methods in Engineering; 2015. p. 1–21.
[32] Thompson M, Hourigan K, Sheridan J. Three-dimensional instabilities in the wake of a circular cylinder. Exp Therm Fluid Sci. 1996;12:190–196.
[33] Scargle JD. Studies in astronomical time series analysis. II. Statistical aspects of spectral analysis of unevenly spaced data. Astrophys J. 1982;263:835–853.
[34] Prasad A, Williamson CHK. Three-dimensional effects in turbulent bluff body wakes. Exp Therm Fluid Sci. 1997;14:9–16.